Composites Science and Technology 177 (2019) 34–40

Contents lists available at ScienceDirect

Composites Science and Technology

journal homepage: www.elsevier.com/locate/compscitech

Quantification of stress transfer in a model cellulose nanocrystal/graphene bilayer using Raman spectroscopy

J.J. Morgan[a], M.F. Craciun[a,*], S.J. Eichhorn[b,**]

[a] College of Engineering, Mathematics and Physical Sciences, University of Exeter, North Park Road, EX4 4QF, Exeter, UK
[b] Bristol Composites Institute (ACCIS), University of Bristol, Queen's Building, University Walk, Bristol, BS8 1TR, UK

ARTICLE INFO

Keywords:
A: Nanocomposites
B: Interfacial strength
D: Raman spectroscopy

ABSTRACT

Graphene and cellulose possess a multitude of unique and useful properties for applications in electronics, sensors and composites which has led to significant scientific interest over the past 5–10 years. Despite this interest, there has been no experimental work investigating the interface or stress transfer efficiency between these materials, which limits future developments in this field. With the aim of investigating this interface, we have created a model bilayer composite, consisting of a tunicate derived cellulose nanocrystal (T-CNC) film and a monolayer of graphene produced by chemical vapour deposition. Raman spectroscopy has been used to monitor the four-point bending of this model bilayer composite. Shifts in the position of Raman bands, unique for both the cellulose and graphene components of this model composite, are recorded. Using a novel analysis of these Raman band shifts, we have formed an expression which deconvolutes the total stress transfer efficiency of the model system. Using this deconvolution, a stress transfer efficiency of 66% has been derived at the cellulose/graphene interface. In addition, splitting of the graphene Raman G band has allowed calculation of the shear strain in the graphene, which is assumed to be equal to that at the cellulose-graphene interface. The individual T-CNCs in the reference samples showed location dependent preferential orientations. The film was found to be stiffer when the T-CNCs were oriented parallel to the loading axis. It was intended that the varying stiffness of the cellulose film could be used to analyse the effects of underlying film stiffness on stress transfer efficiency, but conclusions from this test were limited. The detailed interface analysis presented here will help to inform design in future cellulose/graphene devices.

1. Introduction

Cellulose nanocrystals (CNCs) and graphene have been used together in the fields of functional materials and composite science for the past 5–10 years. Individually they possess desirable properties; graphene boasts high electrical and thermal conductivity in a two dimensional, atomically thin sheet [1,2]. Cellulose is electrically insulating; is a potential biodegradable, renewable, and cheap replacement of oil-based polymers; and can form high aspect ratio, one dimensional nanomaterials [3]. The materials also have several complementary material properties. Both can form flexible films [4], are highly transparent [5], are conformal, have desirable mechanical properties such as high Young's modulus and tensile strengths [6,7], and both are now widely available commercially. Cellulose nanocrystals and graphene have been used to create various composites, including transparent, flexible conductive films [8,9], flexible transparent films for solar cells [5], flexible supercapacitors [10], organic chemical sensors [11], and aerogels [12].

Despite the number of reported composites containing both cellulose and graphene, there has been no experimental determinations of the interfacial bonding and stress transfer efficiency between the two materials. In this work we aim to quantify the stress transfer efficiency of a cellulose/graphene interface. As both graphene and cellulose nanocrystals are too small to test using conventional mechanical testing techniques, micro Raman spectroscopy has been employed. This approach also allows a quantification of the stress-transfer efficiency between the two phases as well as giving information about locally varying mechanical properties.

Raman spectroscopy is a powerful, non-destructive method of studying molecular deformation of polymers [13] and carbonaceous materials [14,15]. The technique was first established for monocrystalline polydiacetylene, where, upon application of a tensile load,

* Corresponding author.
** Corresponding author.
E-mail addresses: m.f.craciun@exeter.ac.uk (M.F. Craciun), s.j.eichhorn@bristol.ac.uk (S.J. Eichhorn).

https://doi.org/10.1016/j.compscitech.2019.04.011
Received 10 December 2018; Received in revised form 8 April 2019; Accepted 11 April 2019
Available online 14 April 2019

the Raman bands associated with the C≡C and C═C bonds decreased in frequency [16]. This discovery has been further developed, and similar stress dependent Raman band shifts have been discovered in other crystalline materials, including cellulose [7] and graphene [17].

In this paper, we use Raman spectroscopy to monitor the shifts in position of characteristic bands during the four-point bending of a bilayer composite, comprising of tunicate derived cellulose nanocrystals (T-CNCs) and monolayer graphene. Both graphene and T-CNC films have high optical transparency. This allows the Raman excitation laser to be focused at the interface of the two materials, allowing a quantification of the stress-transfer efficiency between the two phases.

2. Experimental

2.1. Materials

The cellulose source was 750 g of *Ascidiella aspersa* tunicates, purchased from Loch Fyne Seafarms. Monolayer chemical vapour deposition (CVD) graphene on copper foil was bought from www.graphene-supermarket.com. Two-part epoxy resin substrates were made from Araldite 5052 and Aradur 5052, purchased from Mouldlife. To monitor strain, CEA-06-240UZ-120 Vishay linear strain gauges were used.

2.2. Preparation of tunicate cellulose nanocrystals

A detailed protocol for the preparation of T-CNCs can be found in Ref. [18], which is adapted from Refs. [19,20].

2.3. Electron microscopy of T-CNCs

T-CNCs were imaged using a 120 kV JEOL JEM 1400 transmission electron microscope (TEM) by depositing a droplet of a 0.02 wt% aqueous suspension onto a holey carbon copper TEM grid. The T-CNCs were negatively stained with uranyl acetate and imaged. TEM images and their analysis can be found in Supplementary Information (§S1).

2.4. Characterisation of graphene

The graphene was transferred onto a silicon substrate and characterised using Raman spectroscopy, according to the methodology in Ref. [21] (see Supplementary Information, §S2).

2.5. Production of model composites

Four types of sample were created (Fig. 1a); a T-CNC reference (T-CNC), a graphene reference (G), and two bilayers, one bilayer where the graphene is deposited first with the cellulose deposited on top (G/T-CNC) and one bilayer where the T-CNC is deposited first with the graphene deposited on top (T-CNC/G). Three of each of the different sample types were created, totalling 12 samples.

Epoxy resin substrates were created from a 50:19 wt ratio of Araldite 5052 to Aradur 5052. The substrates were cut into 70 × 22 × 3 mm beams using a laser cutter. Strain gauges were attached to the underside of these beams. Compressive strains on the underside of the substrate were equated to tensile strain on the top side. The T-CNC ref. sample was created by depositing 0.1 mL of 1.8 wt% aqueous solution of T-CNCs onto the substrates. The solution was spread out to form a circular droplet of 1 cm in diameter. The substrate and droplet were placed in a vacuum of 750 mBar below atmospheric pressure for 8 h, with a permanent magnet (0.6 T) on either side of substrate (Fig. 1b). In preliminary testing, the use of magnets appeared to improve the formation and consistency of oriented T-CNC films. The precise mechanism underlying this behaviour has not been investigated here but similar work involving magnetic orientation of CNCs can be found elsewhere [22,23]. The vacuum was used to speed up the drying process.

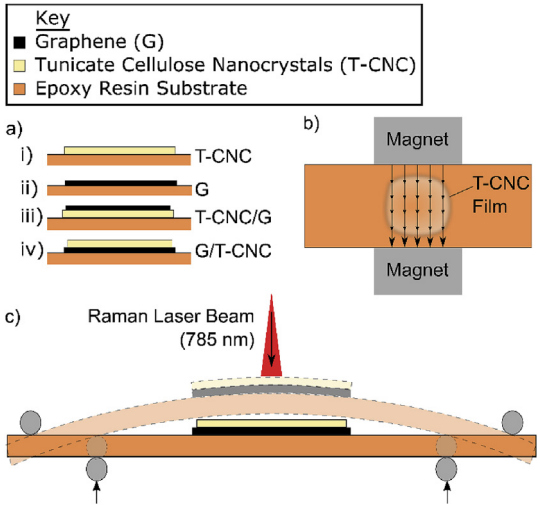

Fig. 1. Schematic of (a) the four different sample types, showing i) tunicate cellulose nanocrystal (T-CNC) reference, ii) graphene (G) monolayer reference iii) T-CNC/G bilayer iv) G/T-CNC bilayer. (b) Plan view of T-CNC film drying in a magnetic field. Arrows indicate field direction. (c) Four-point bending test. Images not to scale.

Graphene reference samples (G ref.) were prepared by transferring the CVD graphene onto a substrate, following the transfer methodology used in Ref. [21]. Bilayer samples were created by following the same deposition methods described previously. For the T-CNC/G bilayer sample, the cellulose was deposited first and graphene second and *vice versa* for the G/T-CNC bilayer. In each of the bilayers the top layer was deposited in such a way that it only contacted the bottom layer and did not contact the epoxy resin substrate. This ensured that the top material in the bilayer only experienced stress transfer between the graphene and the layer of cellulose and was not 'pinned' by an interaction with the epoxy resin substrate.

It was found that for all the G/T-CNC samples, the T-CNC film spontaneously started to debond from the graphene shortly after the sample was removed from the vacuum chamber. These samples were deemed unusable in the four-point bending tests, as the films had completely separated before any load could be applied. The implications of this observation are discussed later.

2.6. Raman spectroscopy

Raman spectroscopy was performed on a RM1000 Renishaw Raman spectrometer, using a 785 nm laser focussed through a 50 × objective lens onto the sample surface. Before testing, the spectrometer was calibrated using a silicon standard.

2.6.1. Angle dependent Polarised Raman spectroscopy

Polarised Raman spectroscopy was used to determine the orientation of the T-CNC film. The incident light was polarised parallel to the front edge of the microscope stage and the backscattered light was passed through an analyser oriented in the same direction, commonly referred to as a vertical-vertical (VV) polarisation setup. The epoxy resin substrates were initially oriented so that their long edge was parallel to the loading direction. Raman spectra were obtained using four accumulations with an exposure time of 20 s per accumulation. The orientation of the model composites was rotated between 0° and 360° in increments of 10°, taking Raman spectra at each interval. A recognisable visual marker on the T-CNC film was used to scan the exact same position each time.

2.6.2. Micromechanics of model composites under four-point bending

Four-point bending tests were performed on the three sample types

while being monitored using the Raman spectrometer (Fig. 1c). Samples were deformed in a cycle (load, unload, second load) between 0 and 0.5% strain. Raman spectra were taken at 0.025% intervals of strain during this cycle. Three spectroscopic areas of interest were scanned; 1040–1140 cm^{-1}, 1540–1640 cm^{-1}, and 2500–2660 cm^{-1} which incorporate the cellulose band initially located at ~1095 cm^{-1} band, the graphene G band and 2D band respectively.

For the T-CNC ref. samples the laser was used at maximum power (100%). The laser power was reduced (to 33%) for the G ref. and T-CNC/G bilayer samples to avoid beam damage and heating effects. Samples were exposed for the same time-period as for the orientation studies. Where a Raman band exhibited a poor signal to noise ratio, the number of accumulations for that region was doubled, but the sampling interval was reduced to every 0.04% strain increment. This increased scan quality but reduced the number of data acquired.

Two polarisation conditions were used; namely VV and vertical-horizontal (VH). The VV polarisation condition has already been described. The VH condition is identical, but with the addition of a half waveplate being placed ahead of the analyser. A visual marker on the surface of the samples was used to locate the exact same position for each scan. This visual marker was either; in the region above the centre of the T-CNC film, where the T-CNCs are later demonstrated to be mainly parallel to the loading axis; or in the region to the right of the centre of the T-CNC film, where the T-CNCs are demonstrated to mainly perpendicular to the loading axis (see Fig. 2c); herein these regions will be labelled parallel and perpendicular respectively. The graphene showed no preferential orientation, so the initial scan location was arbitrarily chosen; regardless, the exact position of this initial scan was used for the remainder of the test.

2.6.3. Raman spectra peak fitting

A detailed analysis of the fitting of the Raman bands can be found in Supplementary Information (§S3). It is important to note that the graphene G band has been extracted from degenerate epoxy resin peaks.

2.6.4. Raman drift correction

The peak positions of the Raman band initially located at ~1095 cm^{-1} have been adjusted to account for drift in the experiments. A detailed explanation of the drift and how it has been corrected can be found in Supplementary Information (§S4).

2.6.5. Determining hydrostatic and shear strain in graphene using vector map analysis

Shifts in the position of the graphene G and 2D bands can either be the result of changes in doping or in strain. Lee et al. developed a method for separating strain and charge doping effects in graphene [17] which was later improved by Mueller et al. [24]. This method has been employed here; see Supplementary Information (§S5) for a brief overview of the topic. Specific adaptations have been made to the original methodology which are detailed in Supplementary Information (§S6); the validity of these adaptations is also discussed there.

3. Results and discussion

3.1. T-CNC characterisation

Data from the angular dependent polarised Raman spectroscopy test are shown in Fig. 2. Data have been fitted with the equation

$$I = A_1 \cos^4(\theta + \varphi) + A_2 \cos^4(\theta + 90° + \varphi) + C \quad (1)$$

where I is the normalised Raman intensity, θ is the film orientation angle, and A_1, A_2, φ, and C are fitting parameters. Similar polarised Raman spectroscopy experiments have been performed on flax fibres [25] and the equation used to fit those data was of the form

$$I = A_1 \cos^4(\theta + \varphi) + C \quad (2)$$

In equation (2), a large ratio between A_1: C indicated a high degree of fibre orientation, a low ratio indicated random orientation, and an angle φ indicated the direction of orientation. In the present work, a smaller secondary cosine function (perpendicular to the primary cosine

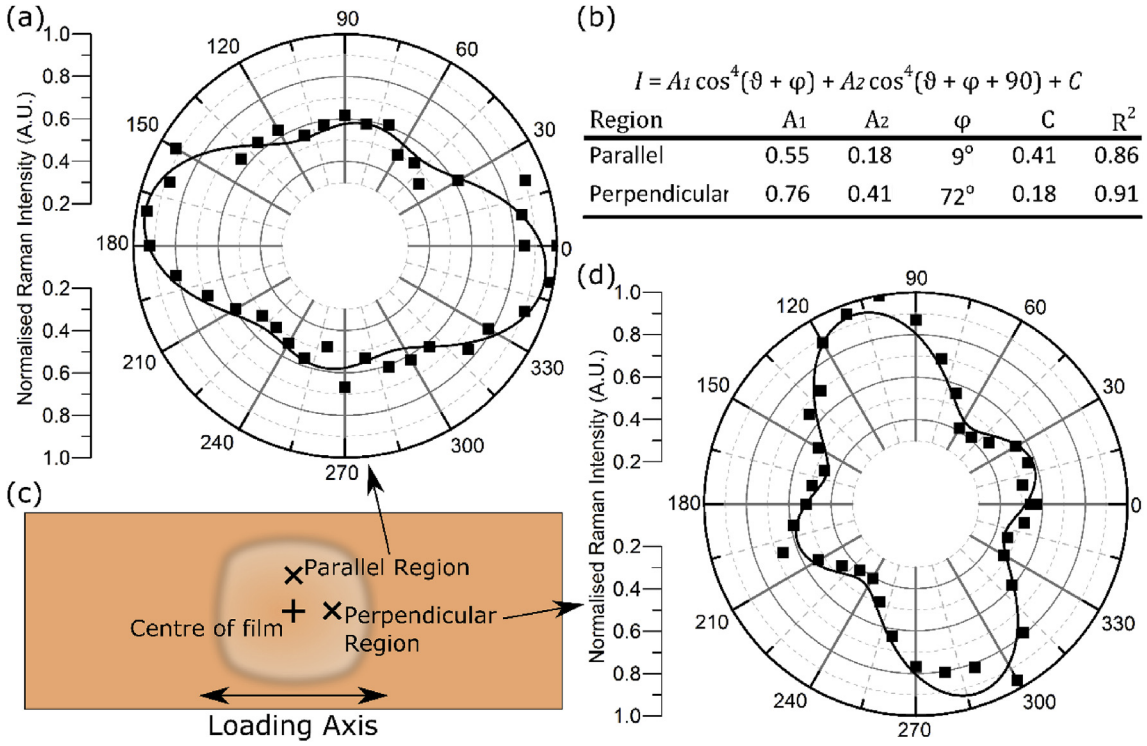

Fig. 2. (a) Normalised intensity of the Raman band located at ~1095 cm^{-1} as a function of sample orientation. Data were collected in the parallel region of the sample. (b) Summary of the fitting parameters A_1, A_2, φ, and C. (c) Schematic of the cellulose film highlighting the scanned regions. (d) Same as '(a)' but for the perpendicular region.

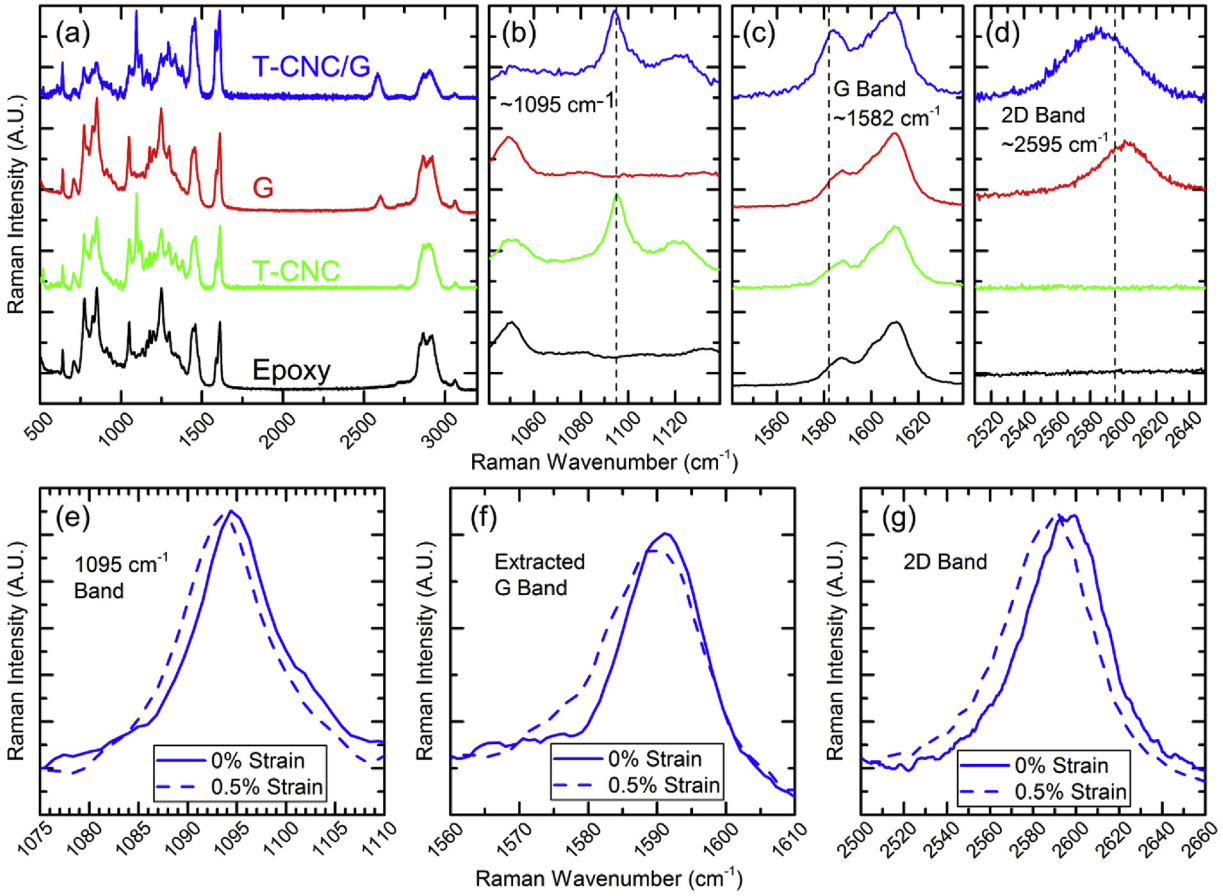

Fig. 3. (a) Full Raman spectra (at 0% strain) of the epoxy resin substrate, tunicate cellulose nanocrystal (T-CNC) reference, graphene (G) reference and T-CNC/G bilayer. The same data is shown on rescaled axes highlighting the three characteristic Raman bands of interest (b) cellulose located at ~1095 cm^{-1}, (c) graphene G, (d) graphene 2D. A comparison of T-CNC/G Raman spectra at 0% and 0.5% strain for the (e) band initially located at ~1095 cm^{-1}, (f) extracted G band, and (g) 2D band.

function) is present. This secondary function has appeared in other published work [25,26], but its origin has not been explained. It may be related to the tendency of T-CNCs to form chiral nematic structures, although more work is needed to confirm this.

Fig. 2a and d show that the orientation of the fibres is location dependent. Based on the primary cosine function, the data indicates that the T-CNCs in the region above the centre of the model composites are oriented preferentially parallel to the loading axis. In the region right of the centre of the composite they are oriented preferentially perpendicular to the loading axis.

3.2. Raman monitored four-point bending test

Fig. 3 (a-d) shows Raman spectra for each of the tested samples. Both the band located at ~1095 cm^{-1} and the 2D band, in Fig. 3b and d respectively, are well-resolved, and do not have any degenerate peaks. Upon application of tensile deformation, both these bands shift to a lower wavenumber position as indicated in Fig. 3e and g. Unfortunately, the G band has degenerate bands with the epoxy resin, as shown in Fig. 3c. Despite this, the data processing, which extracts the G band from the combined peaks, produces a well-resolved Raman band. This band also shifts with applied deformation (Fig. 3f).

The following section analyses the how characteristic Raman bands change with respect to applied load. The notation '$\omega_{[\,]}$' refers to the peak position of a Raman band, where the subscript indicates which band is of interest; 'T-CNC' for the cellulose 1095 cm^{-1} band, or 'G' or '2D' for the graphene G and 2D bands respectively (see Supplementary information §S3 and §S5 for why $\overline{\omega_G}$ is averaged). The notation '$\varepsilon_{[\,]}$' refers to strain. This can refer to either the input strain (the value read from the strain gauge – the controlled variable) or the measured strain in the graphene (calculated using the vector map analysis); these use the subscripts '*In*' and '*Mea*' respectively. Finally, measured strain always uses a superscript '$\varepsilon^{[\,]}_{Mea}$'; '*H*' for hydrostatic strain, or 'τ' for shear strain.

Fig. 4a shows how ω_{T-CNC} changes with respect to ε_{In}. For both the T-CNC and T-CNC/G samples, $d\omega_{T-CNC}/d\varepsilon_{In}$ is constant and has recoverable linear deformation. This is consistent with loading a sample in the elastic region of the stress strain curve. For the T-CNC samples, average $d\omega_{T-CNC}/d\varepsilon_{In} = -1.90 \pm 0.48$ cm^{-1} $\%^{-1}$. In a similar test using a T-CNC sheet embedded in epoxy resin, Šturcová et al. measured $d\omega_{T-CNC}/d\varepsilon_{In} = -2.4 \pm 0.2$ cm^{-1} $\%^{-1}$. As their shift rate was measured in a fully encased system rather than as simply supported system (as in the present approach), it is reasonable to expect a reduction in stress transfer efficiency and hence a reduction in shift rate with respect to strain.

Fig. 4b plots ε^{H}_{Mea} against ε_{In}. Similarly, Fig. 4c plots ε^{τ}_{Mea} against ε_{In}; in both cases there is a recoverable linear relationship between the two. Data in Fig. 4c has a much larger standard deviation because ε^{τ}_{Mea} is entirely calculated using the extracted G band, which has considerable variation (likely due to the extraction process).

For all cellulose films the relationship between ε_{In} and ω_{T-CNC} is linear. Fig. 5a shows a bar chart summarising these gradients ($d\omega_{T-CNC}/d\varepsilon_{In}$) for different samples, scan locations and polarisation configurations. Likewise, for the graphene, in all samples there is a linear relationship between both; ε_{In} and ε^{H}_{Mea}, and ε_{In} and ε^{τ}_{Mea}. These gradients, $d\varepsilon^{H}_{Mea}/d\varepsilon_{In}$ and $d\varepsilon^{\tau}_{Mea}/d\varepsilon_{In}$, are plotted in Fig. 5b and c respectively, where different samples and scanned regions are compared.

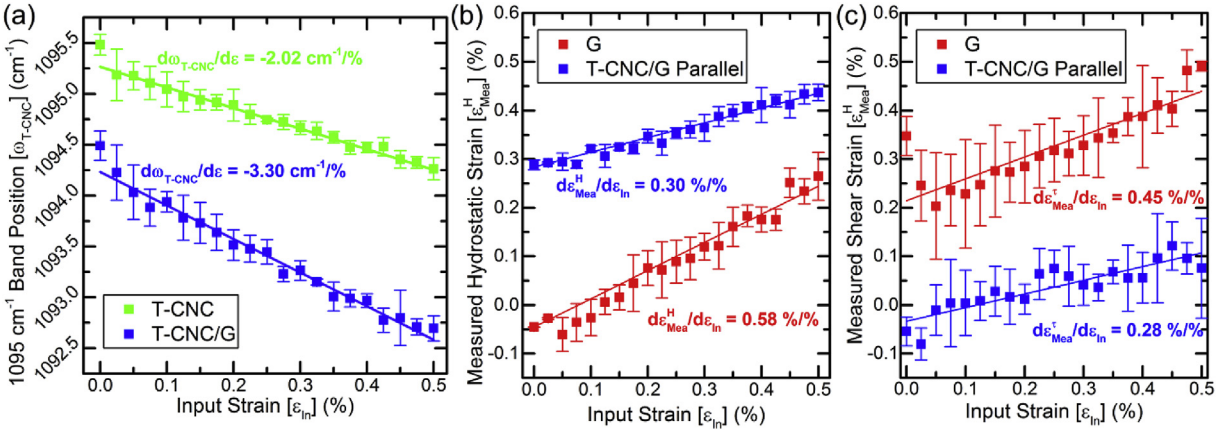

Fig. 4. (a) Position of the Raman band initially located at ~1095 cm^{-1} (ω_{T-CNC}) with respect to strain (ε_{In}), for a representative T-CNC and T-CNC/G sample (parallel region; VV polarisation). Measured (b) hydrostatic (ε^{H}_{Mea}) and (c) shear (ε^{τ}_{Mea}) strain against ε_{In} for representative G and T-CNC/G samples. Each datum is an average of the load, unload and second load. Error bars are standard deviations from the mean.

In Fig. 5a–c, it should be noted that the bar heights only consider the respective gradients and do not show the initial conditions (they do not show initial values of ω_{T-CNC} ε^{H}_{Mea}, or ε^{τ}_{Mea}), of which there are differences; see Fig. 4b, in which the ε^{H}_{Mea} values at ε_{In} = 0% are drastically different for the G and T-CNC/G samples. This is not represented in Fig. 5b. Additionally, in Fig. 5b and c, the error bars only represent the standard deviation of $d\varepsilon^{H}_{Mea}/d\varepsilon_{In}$ and $d\varepsilon^{\tau}_{Mea}/d\varepsilon_{In}$ for the three samples. They do not consider the error in the $\overline{\omega_G}$ or ω_{2D} data, where some data sets, particularly the extracted G band data, have a large spread.

Fig. 5a–c show two statistically strong trends and one weak trend. There is a strong trend in Fig. 5b, the average $d\varepsilon^{H}_{Mea}/d\varepsilon_{In}$ in the parallel T-CNC/G data is smaller than for the G reference. Additionally, in Fig. 5a, the value of $d\omega_{T-CNC}/d\varepsilon_{In}$ is larger for the T-CNC/G samples than for the T-CNC references. Finally, there is a weak trend in Fig. 5a, where the T-CNC reference exhibits a greater value of $d\omega_{T-CNC}/d\varepsilon_{In}$ in the parallel region than for the perpendicular region.

The differences in $d\varepsilon^{H}_{Mea}/d\varepsilon_{In}$ can be explained by stress transfer efficiencies. In the T-CNC/G model system, load is applied to the epoxy resin substrate and stress is transferred through various material interfaces to the graphene on the top layer. At various points, there will be losses in this system, where stress is not transferred between phases, or is lost through some other mechanism. We can quantify these losses using stress transfer efficiencies.

Equation (3) is an expression for the total stress transfer efficiency (η_{Total}), which can describe the bilayer model when tested in the parallel region. It has been deconvoluted into three stress transfer efficiency components ($\eta_{Wrinkles}$, η_{T-CNC} and $\eta_{Interface}$). These efficiency components are cumulative according to the equation:

$$\eta_{Total} = \eta_{Wrinkles} \times \eta_{T-CNC} \times \eta_{Interface} \quad (3)$$

η_{Total} can be determined from Fig. 5b, using $d\varepsilon^{H}_{Mea}/d\varepsilon_{In}$ for the parallel region. $d\varepsilon^{H}_{Mea}/d\varepsilon_{In}$ is effectively a measure of stress transfer, as it represents the proportion of the input strain which can be measured as hydrostatic strain in the graphene; namely 29%.

The first stress transfer efficiency component is the result of wrinkles in the graphene ($\eta_{Wrinkles}$). Raman studies, which use characteristic band shift rates to determine graphene stiffness, have shown that the stiffness of CVD graphene is greatly reduced in comparison to pristine mechanically exfoliated graphene [27]. The reduction in stiffness was attributed to wrinkles in the CVD graphene structure. Upon application of a tensile load, these wrinkles would move and unfold. This deformation of the wrinkles would not be detected using the Raman spectroscopic approach, as it does not directly deform the carbon-carbon bonds. $\eta_{Wrinkles}$ can be quantified using $d\varepsilon^{H}_{Mea}/d\varepsilon_{In}$ for the G Ref.

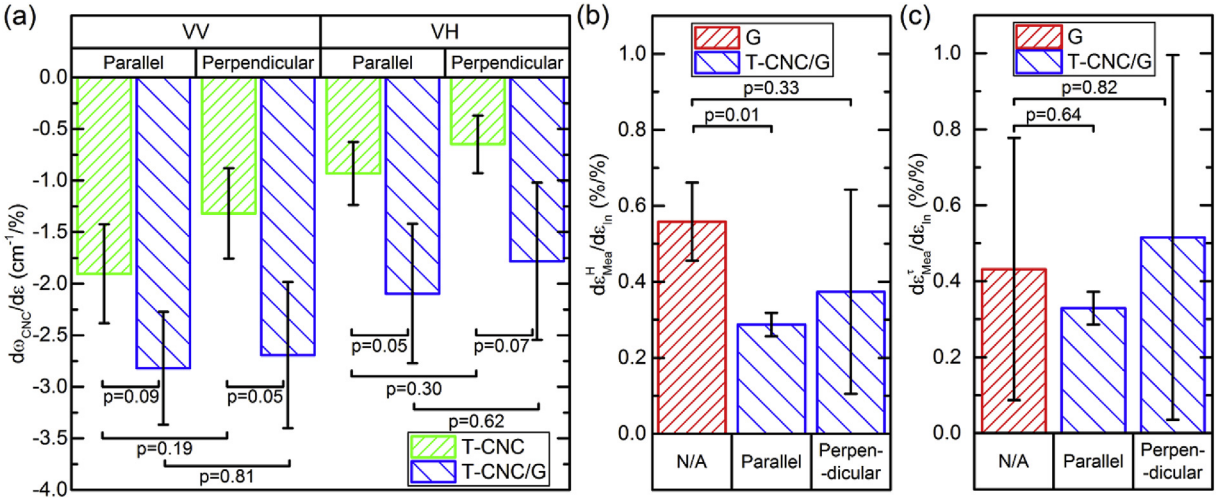

Fig. 5. (a) Cellulose Raman band shift rates for different sample types in different scan locations; Comparison of (b) the change in measured hydrostatic strain in graphene as a function of input strain ($d\varepsilon^{H}_{Mea}/d\varepsilon_{In}$), and (c) the change in measured shear strain in graphene as a function of input strain ($d\varepsilon^{\tau}_{Mea}/d\varepsilon_{In}$), for different sample types in different scan locations. For all graphs, the bar heights show the average values of the first load, unload and second load for three individual samples (totalling 9 linear fits); error bars represent standard deviations from the mean (n = 3). Square brackets indicate which data have been statistically compared using a two-tailed independent *t*-test, with their calculated p-values given.

samples, where, if we assume that all losses are due to wrinkles in the graphene, we find an efficiency of 56%.

There will also be losses at the epoxy/cellulose interface (η_{T-CNC}). In the T-CNC samples, $d\omega_{T-CNC}/d\varepsilon_{In}$ for the parallel VV test can be compared to work by Šturcová et al., who tested T-CNCs fully embedded in epoxy resin. The shift rate in the fully embedded system was $-2.4\,cm^{-1}\,\%^{-1}$, compared to $-1.90\,cm^{-1}\,\%^{-1}$ in this work (Fig. 5a). Taking the fully embedded system as a benchmark, the stress transfer efficiency of the epoxy/cellulose interface in the present work is 79%. The loss in efficiency can be explained by a reduction in contact area; the T-CNC film is a network of fibres with a rough surface, which is in contact with a smooth, flat substrate. Inevitably the contact area is reduced compared to cellulose fully embedded in epoxy resin.

The final stress transfer efficiency component is due to the losses at the cellulose/graphene interface ($\eta_{Interface}$). Determining $\eta_{Interface}$ is the objective of this research. We have already determined η_{Total} (29%), $\eta_{Wrinkles}$ (56%) and η_{T-CNC} (79%). If we assume that all remaining losses in this model system are a result of the cellulose/graphene interface, then using Equation (3), we find a stress transfer efficiency at this interface of 66%.

So far, only the parallel region data have been considered. A network of one-dimensional fibres tends to be stiffer when the fibres are aligned parallel to the loading axis. The T-CNCs show location dependent orientations, both parallel and perpendicular to the loading axis. Fig. 5a shows a weak trend in the T-CNC reference data, where the parallel region exhibits a greater value of $d\omega_{T-CNC}/d\varepsilon_{In}$ than the perpendicular region. This confirms that the T-CNC film is stiffer where the fibres are aligned parallel to the loading axis. It was intended that by performing tests in both parallel and perpendicular regions we could compare the effects of underlying film stiffness on the efficiency of stress transfer; however, in the bilayer sample, there is no statistically significant difference between the stiffnesses of the parallel and perpendicular regions of the T-CNC film. This results in approximately the same $d\varepsilon^{H}_{Mea}/d\varepsilon_{In}$ for the parallel and perpendicular regions (Fig. 5b); this comparison would be closer in size, but one sample has skewed the perpendicular data upwards. Any further analysis of the parallel and perpendicular regions is limited.

In Fig. 5a, there is a strong trend, where $d\omega_{T-CNC}/d\varepsilon_{In}$ is larger for the T-CNC/G data than the corresponding T-CNC data. A possible explanation for the difference is the amount of water absorbed in the T-CNC film. Previous research has shown that the act of wetting a CNC film reduced shift rates of the cellulose Raman band ($1095\,cm^{-1}$) from $-0.5\,cm^{-1}/\%$ to $\sim 0\,cm^{-1}/\%$ [28]. In the present work, the final stage of the T-CNC sample preparation is 8 h in a vacuum. In the T-CNC/G samples, the final stage is the wet transfer of graphene, where the recently transferred, wet CNC/graphene/PMMA structure is placed in a vacuum for 2 h, before gentle heating in acetone to remove the PMMA layer. In both situations after the samples have been thoroughly dried in a vacuum, they are left exposed to the atmosphere. In the T-CNC samples the cellulose is completely exposed, but in the T-CNC/G samples the graphene acts as an impermeable barrier to gas/liquids [29]. If the T-CNC samples absorb a small amount of water from the atmosphere, then this might reduce $d\omega_{T-CNC}/d\varepsilon_{In}$ in comparison to the protected T-CNC film in the T-CNC/G samples.

Finally, Fig. 5c compares measured shear strain in the graphene. Unfortunately, there is no statistically significant trends in this data, which is due to very large standard deviations and a small sample size. The exceptionally long time it takes to complete a full cycle of testing for a single sample prevents larger sample sizes using this methodology. An alternative method would be to assume that the changes in Raman bands between 0% strain and 0.5% strain are always linear in the present work, all samples have shown linear changes. One would then be able to perform a Raman map at 0% strain, and then perform a map of the same area at 0.5% strain. Pointwise pairing of the data at 0% strain and 0.5% strain would provide all the necessary information needed for interface analysis, whilst drastically increasing the sample size.

4. Conclusions

Using Raman spectroscopy, we have quantified a stress transfer efficiency of 66% at the interface of a tunicate cellulose nanocrystal film and a graphene monolayer. Additionally, we have performed this test with the tunicate cellulose nanocrystals oriented both parallel and perpendicular to the loading axis. Although the T-CNC films in the reference showed location dependent stiffnesses, in the bilayer, this variation disappeared. This limited analysis of these regions. Observed differences in the cellulose Raman band shift rates, between sample types, may arise from the preparation methods used and the presence of moisture.

Acknowledgements

We acknowledge financial support from the Engineering and Physical Sciences Research Council (EPSRC) of the United Kingdom, via the EPSRC Centre for Doctoral Training in Metamaterials (Grant No. EP/L015331/1). All data created during this research are openly available from the University of Exeter's institutional repository at ***INSERT OPEN ACCESS DOI LINK HERE***

Appendix A. Supplementary data

Supplementary data to this article can be found online at https://doi.org/10.1016/j.compscitech.2019.04.011.

References

[1] K.S. Novoselov, A.K. Geim, S.V. Morozov, D. Jiang, Y. Zhang, S.V. Dubonos, I.V. Grigorieva, A.A. Firsov, Electric field effect in atomically thin carbon films, Science (80-.) 306 (2004) 666–669, https://doi.org/10.1126/science.1102896.
[2] A.K. Geim, K.S. Novoselov, The rise of graphene, Nat. Mater. 6 (2007) 183–191, https://doi.org/10.1038/nmat1849.
[3] E.J. Foster, R.J. Moon, U.P. Agarwal, M.J. Bortner, J. Bras, S. Camarero-Espinosa, K.J. Chan, M.J.D. Clift, E.D. Cranston, S.J. Eichhorn, D.M. Fox, W.Y. Hamad, L. Heux, B. Jean, M. Korey, W. Nieh, K.J. Ong, M.S. Reid, S. Renneckar, R. Roberts, J.A. Shatkin, J. Simonsen, K. Stinson-Bagby, N. Wanasekara, J. Youngblood, Current characterization methods for cellulose nanomaterials, Chem. Soc. Rev. 47 (2018) 2609–2679, https://doi.org/10.1039/c6cs00895j.
[4] K.K. Sadasivuni, A. Kafy, L. Zhai, H.U. Ko, S. Mun, J. Kim, Transparent and flexible cellulose nanocrystal/reduced graphene oxide film for proximity sensing, Small 11 (2015) 994–1002, https://doi.org/10.1002/smll.201402109.
[5] L. Valentini, S. Bittolo Bon, E. Fortunati, J.M. Kenny, Preparation of transparent and conductive cellulose nanocrystals/graphene nanoplatelets films, J. Mater. Sci. 49 (2014) 1009–1013, https://doi.org/10.1007/s10853-013-7776-9.
[6] G.-H. Lee, R.C. Cooper, S.J. An, S. Lee, A. van der Zande, N. Petrone, A.G. Hammerberg, C. Lee, B. Crawford, W. Oliver, J.W. Kysar, J. Hone, High-Strength chemical-vapor-deposited graphene and grain boundaries, Science 80 (340) (2013) 1073–1076, https://doi.org/10.1126/science.1235126.
[7] A. Šturcová, G.R. Davies, S.J. Eichhorn, Elastic modulus and stress-transfer properties of tunicate cellulose whiskers, Biomacromolecules 6 (2005) 1055–1061, https://doi.org/10.1021/bm049291k.
[8] F. Wang, L.T. Drzal, Y. Qin, Z. Huang, Multifunctional graphene nanoplatelets/cellulose nanocrystals composite paper, Compos. B Eng. 79 (2015) 521–529, https://doi.org/10.1016/j.compositesb.2015.04.031.
[9] S. Montes, P.M. Carrasco, V. Ruiz, G. Cabañero, H.J. Grande, J. Labidi, I. Odriozola, Synergistic reinforcement of poly(vinyl alcohol) nanocomposites with cellulose nanocrystal-stabilized graphene, Compos. Sci. Technol. 117 (2015) 26–31, https://doi.org/10.1016/j.compscitech.2015.05.018.
[10] Z. Weng, Y. Su, D.W. Wang, F. Li, J. Du, H.M. Cheng, Graphene-cellulose paper flexible supercapacitors, Adv. Energy Mater. 1 (2011) 917–922, https://doi.org/10.1002/aenm.201100312.
[11] J. Cao, X. Zhang, X. Wu, S. Wang, C. Lu, Cellulose nanocrystals mediated assembly of graphene in rubber composites for chemical sensing applications, Carbohydr. Polym. 140 (2016) 88–95, https://doi.org/10.1016/j.carbpol.2015.12.042.
[12] X. Zhang, P. Liu, Y. Duan, M. Jiang, J. Zhang, Graphene/cellulose nanocrystals hybrid aerogel with tunable mechanical strength and hydrophilicity fabricated by ambient pressure drying technique, RCS Adv. 7 (2017) 16467–16473, https://doi.org/10.1039/c6ra28178h.
[13] R.J. Young, S.J. Eichhorn, Deformation mechanisms in polymer fibres and nanocomposites, Polymer (Guildf) 48 (2007) 2–18, https://doi.org/10.1016/j.polymer.2006.11.016.
[14] R.J. Young, I.A. Kinloch, L. Gong, K.S. Novoselov, The mechanics of graphene

nanocomposites: a review, Compos. Sci. Technol. 72 (2012) 1459–1476, https://doi.org/10.1016/j.compscitech.2012.05.005.
[15] A.C. Ferrari, D.M. Basko, Raman spectroscopy as a versatile tool for studying the properties of graphene, Nat. Nanotechnol. 8 (2013) 235–246, https://doi.org/10.1038/nnano.2013.46.
[16] V.K. Mitra, W.M. Risen, R.H. Baughman, A laser Raman study of the stress dependence of vibrational frequencies of a monocrystalline polydiacetylene, J. Chem. Phys. 66 (1977) 2731–2736, https://doi.org/10.1063/1.434219.
[17] J.E. Lee, G. Ahn, J. Shim, Y.S. Lee, S. Ryu, Optical separation of mechanical strain from charge doping in graphene, Nat. Commun. 3 (2012) 1024–1028, https://doi.org/10.1038/ncomms2022.
[18] K. Shanmuganathan, J.R. Capadona, S.J. Rowan, C. Weder, Stimuli-responsive mechanically adaptive polymer nanocomposites, ACS Appl. Mater. Interfaces 2 (2010) 165–174, https://doi.org/10.1021/am9006337.
[19] V. Favier, H. Chanzy, J.Y. Cavaillé, Polymer nanocomposites reinforced by cellulose whiskers, Macromolecules 28 (1995) 6365–6367, https://doi.org/10.1021/ma00122a053.
[20] H. Yuan, Y. Nishiyama, M. Wada, S. Kuga, Surface acylation of cellulose whiskers by drying aqueous emulsion, Biomacromolecules 7 (2006) 696–700, https://doi.org/10.1021/bm050828j.
[21] A.J. Pollard, K.R. Paton, C.A. Clifford, E. Legge, A. Oikonomou, S. Haigh, C. Casiraghi, L. Nguyen, D. Kelly, Good Practice Guide No. 145 - Characterisation of the Structure of Graphene, first ed., National Physical Laboratory, 2017.
[22] J. Sugiyama, H. Chanzy, G. Maret, Orientation of cellulose microcrystals by strong magnetic fields, Macromolecules 25 (1992) 4232–4234, https://doi.org/10.1021/ma00042a032.
[23] K.J. De France, K.G. Yager, T. Hoare, E.D. Cranston, Cooperative ordering and kinetics of cellulose nanocrystal alignment in a magnetic field, Langmuir 32 (2016) 7564–7571, https://doi.org/10.1021/acs.langmuir.6b01827.
[24] N.S. Mueller, S. Heeg, M.P. Alvarez, P. Kusch, S. Wasserroth, N. Clark, F. Schedin, J. Parthenios, K. Papagelis, C. Galiotis, M. Kalbáč, A. Vijayaraghavan, U. Huebner, R. Gorbachev, O. Frank, S. Reich, Evaluating arbitrary strain configurations and doping in graphene with Raman spectroscopy, 2D Mater. 5 (2017) 1–9, https://doi.org/10.1088/2053-1583/aa90b3.
[25] S. Tanpichai, F. Quero, M. Nogi, H. Yano, R.J. Young, T. Lindström, W.W. Sampson, S.J. Eichhorn, Effective young's modulus of bacterial and microfibrillated cellulose fibrils in fibrous networks, Biomacromolecules 13 (2012) 1340–1349, https://doi.org/10.1021/bm300042t.
[26] H. Chang, J. Luo, H.C. Liu, A.A. Bakhtiary, P. Wang, S. Kumar, Orientation and interfacial stress transfer of cellulose nanocrystal nanocomposite fibers, Polymer (Guildf) 110 (2017) 228–234, https://doi.org/10.1016/j.polymer.2017.01.015.
[27] Z. Li, I.A. Kinloch, R.J. Young, K.S. Novoselov, G. Anagnostopoulos, J. Parthenios, C. Galiotis, K. Papagelis, C.Y. Lu, L. Britnell, Deformation of wrinkled graphene, ACS Nano 9 (2015) 3917–3925, https://doi.org/10.1021/nn507202c.
[28] R. Rusli, K. Shanmuganathan, S.J. Rowan, C. Weder, S.J. Elchhorn, Stress-transfer in anisotropic and environmentally adaptive cellulose whisker nanocomposites, Biomacromolecules 11 (2010) 762–768, https://doi.org/10.1021/bm1001203.
[29] J.S. Bunch, S.S. Verbridge, J.S. Alden, A.M. Van Der Zande, J.M. Parpia, H.G. Craighead, P.L. McEuen, Impermeable atomic membranes from graphene sheets, Nano Lett. 8 (2008) 2458–2462, https://doi.org/10.1021/nl801457b.